A malignant subpopulation of H2AFZ+ cells interacts with myeloid cells to promote an anti-inflammatory microenvironment and drive hepatic metastasis, revealing an immunotherapeutic strategy for pancreatic ductal adenocarcinoma

Jianyu Yang[1†], Wanhong Chen[2†], Zonghao Duan[1], Minwei Yang[1], Lingye Tao[1], Yanmiao Huo[1], Wei Liu[1], Junfeng Zhang[1], Linli Yao[3], Yingbin Liu[1,3*], Ping Lin[2*], Hong Li[2*] and Yongwei Sun[1,3*]

1 Department of Biliary-Pancreatic Surgery, Ren Ji Hospital, School of Medicine, Shanghai Jiao Tong University, Shanghai 200127, China

2 Shanghai Institute of Nutrition and Health, University of Chinese Academy of Sciences, Chinese Academy of Sciences, Shanghai 200031, China

3 State Key Laboratory of Systems Medicine for Cancer, Shanghai Cancer Institute, Ren Ji Hospital, School of Medicine, Shanghai Jiao Tong University, Shanghai 200240, China

† Jianyu Yang and Wanhong Chen contributed equally to this work.

Running Title: Single-cell transcriptome analysis of metastatic PDAC

*** Corresponding Authors:**

Yongwei Sun, Ren Ji Hospital, School of Medicine, Shanghai Jiao Tong University, 160 Pujian Road, Shanghai 200127, China. Email: syw0616@126.com

Hong Li, Shanghai Institute of Nutrition and Health, University of Chinese Academy of Sciences, Chinese Academy of Sciences, 320 Yueyang Road, Shanghai 200031, China. Email: lihong01@sibs.ac.cn

Ping Lin, Shanghai Institute of Nutrition and Health, University of Chinese Academy of Sciences, Chinese Academy of Sciences, 320 Yueyang Road, Shanghai 200031, China. Email: linping@sinh.ac.cn

Yingbin Liu, Ren Ji Hospital, School of Medicine, Shanghai Jiao Tong University, 160 Pujian Road, Shanghai 200127, China. Email: laoniulyb@shsmu.edu.cn

Conflict of Interest:

The authors declare no potential conflicts of interest.

Downloaded from http://aacrjournals.org/clincancerres/article-pdf/doi/10.1158/1078-0432.CCR-25-3359/3748227/ccr-25-3359.pdf by guest on 01 April 2026

Translational Relevance

Pancreatic ductal adenocarcinoma (PDAC) is a highly lethal malignancy, with nearly half of patients developing distant metastases. The liver is the most frequent metastatic site, and hepatic metastasis is associated with particularly poor outcomes, underscoring the urgent need to elucidate mechanisms that drive metastatic progression. Tumor cells, as the fundamental drivers of metastasis, represent the most critical and central cell population to investigate in metastatic PDAC. By applying single-cell RNA sequencing to paired primary tumors and hepatic metastases, and integrating bulk transcriptomic and pathological data from large patient cohorts, we identify a metastasis-associated tumor subpopulation C2 and its signature gene *H2AFZ* linked to metastatic potential. Targeting *H2AFZ* markedly suppresses the formation of hepatic metastases, highlighting its essential role in metastatic progression and underscoring the translational importance of our findings.

Downloaded from http://aacrjournals.org/clincancerres/article-pdf/doi/10.1158/1078-0432.CCR-25-3359/3748227/ccr-25-3359.pdf by guest on 01 April 2026

Abstract

Purpose: Hepatic metastasis is the leading cause of death in pancreatic ductal adenocarcinoma (PDAC). However, the underlying cellular and molecular programs remain poorly understood, leading to limited therapeutics for this disease.

Experimental Design: Here, we integrated single-cell RNA sequencing data from paired primary tumors (PTs) and hepatic metastases (HMs), along with bulk RNA sequencing and immunohistochemistry data from hundreds of patients to elucidate metastasis-associated programs.

Results: Our analysis identified a metastasis-prone malignant subpopulation, which is associated with a higher risk of hepatic metastasis and a transitional plastic state. This malignant subpopulation represents a poorly differentiated and highly proliferative phenotype, with *H2AFZ* potentially contributing to this phenomenon. Moreover, the presence of tumor cells in the liver was accompanied by an increased abundance of M2 macrophages, regulatory T cells, and exhausted T cells in HMs compared with adjacent tissues, indicative of a shift toward an immune suppressive environment. Notably, within the tumor environment of HMs, exhausted T cells exhibited elevated expression of *PDCD1* and *LAG3*. The combined therapy targeting these two genes effectively inhibited tumor growth in mouse models of metastatic PDAC.

Conclusions: In conclusion, we reveal a metastasis-associated malignant subpopulation and provide a promising therapeutic strategy for metastatic PDAC.

Downloaded from http://aacrjournals.org/clincancerres/article-pdf/doi/10.1158/1078-0432.CCR-25-3359/3748227/ccr-25-3359.pdf by guest on 01 April 2026

Introduction

Pancreatic ductal adenocarcinoma (PDAC) is a highly aggressive and lethal malignancy, characterized by the rapid dissemination of tumor cells. Nearly 50% of PDAC patients present with distant metastases at the time of diagnosis (1). The lack of effective treatments to inhibit metastasis results in a devastating 5-year survival rate of only 3% for these patients (1). Despite the development of new chemotherapy regimens (2,3), targeted therapies (4), and immunotherapies (5)—including NALIRIFOX, olaparib, and PD1/PDL1 inhibitors—the survival benefits for patients with metastatic PDAC remain very limited. This is primarily due to inadequate understanding of the complex mechanisms governing metastatic pancreatic tumors and their interaction with the surrounding microenvironment.

Among all metastatic organs, the liver is the most frequent site of metastasis, and patients with hepatic metastases (HMs) exhibit poorer clinical outcomes (6,7). This underscores the necessity of elucidating the mechanisms underlying hepatic metastasis in PDAC. Our previous work was among the first to explore hepatic metastases and their matched primary tumors (PTs) via bulk RNA sequencing (bulkRNA-seq) and whole-exome sequencing (WES), revealing key features such as altered microenvironments, metabolic rewiring in metastatic PDAC (8). However, the bulk sequencing techniques used in this study were unable to track alterations at the cellular level, limiting the ability to dissect the heterogeneity and dynamic states of individual cells.

The emergence of single-cell RNA sequencing technology (scRNA-seq) offers a great opportunity to explore the underlying molecular and cellular mechanisms at an unprecedented single-cell resolution. This technology has been widely utilized to investigate tumor metastasis in several cancers, such as colon (9), head and neck (10) and gallbladder cancer (11). In pancreatic cancer, scRNA-seq has also been applied on metastatic PDAC (12-14). While these works have advanced our understanding of PDAC metastasis, they primarily emphasized microenvironmental shifts. The intrinsic properties of tumor epithelial cells—the fundamental drivers of metastasis—remain insufficiently explored. In our study, we hope to place a stronger focus on delineating tumor cell subpopulations and their intrinsic roles in driving metastatic progression.

Therefore, we applied scRNA-seq to 12 synchronously resected samples of paired primary tumors and oligo-hepatic metastases. We further integrated bulk RNA-seq and immunohistochemistry (IHC) data from hundreds of PDAC patients to investigate associations between specific cell subsets and metastatic potential. The functional relevance of key cell types and genes was validated through *in vitro* assays using human PDAC cell lines and *in vivo* experiments in murine models. Notably, we observed an enhanced anti-tumor effect of combined anti-PD1 and anti-LAG3 therapy in metastatic mouse models. In summary, our investigation of paired PTs and HMs at single-cell resolution reveals metastasis-associated gene and cellular programs, providing new insights into metastatic mechanisms and offering a promising therapeutic strategy for metastatic PDAC.

Downloaded from http://aacrjournals.org/clincancerres/article-pdf/doi/10.1158/1078-0432.CCR-25-3359/3748227/ccr-25-3359.pdf by guest on 01 April 2026

Materials and Methods

Sample acquisition

A total of 12 fresh samples were obtained from 6 patients (P1-P6) via surgical resection at Shanghai Renji Hospital under institutional review board approval. All patients were pathologically diagnosed as PDAC with liver oligo-metastases. Written informed consent was obtained from all participants before sample collection for research purposes. This study complied with the Helsinki Declaration. Five out of six patients (P1-3, P5-6) had no prior treatment before surgery, whereas P4 had been treated with paclitaxel and gemcitabine before the operation. The detailed clinical information of these patients in this study is provided in Table S1.

The criteria in our study for patients with liver oligo-metastases were based on a previous report (15) as follows: 1) no extrahepatic metastases; 2) not combined with venous resection or multi-visceral resection, and R0 resection can be performed in the primary pancreatic tumor; 3) the number of liver metastases $\leqslant 3$ and macroscopic liver metastases can be completely extirpated by operation or operation combined with radiofrequency ablation; 4) the general medical condition of the patient was good with American Society of Anesthesiologists (ASA) score $\leqslant$ III.

Single-cell RNA library preparation and sequencing

Tissues from 12 paired primary tumors and liver metastases were digested via the dissociation enzyme 0.25% Trypsin (Thermo Fisher, Cat. no.25200-072) and 10 μg/mL DNase I (Sigma, Cat. no. 11284932001). Then, tissues were dissociated at 37 ℃ with a shaking speed of 50 r.p.m for about 40 min. Cell suspensions were filtered using a 40um nylon cell strainer and red blood cells were removed by 1X Red Blood Cell Lysis Solution (Thermo Fisher, Cat. no. 00-4333-57). Cells were stained with 0.4% Trypan blue (Thermo Fisher, Cat. no. 14190144) to check the viability on Countess® II Automated Cell Counter (Thermo Fisher). 10× library preparation and sequencing Beads with unique molecular identifier (UMI) and cell barcodes were loaded close to saturation, so that each cell was paired with a bead in a Gel Beads-in emulsion (GEM). After exposure to cell lysis buffer, polyadenylated RNA molecules hybridized to the beads. Beads were retrieved into a single tube for reverse transcription. On cDNA synthesis, each cDNA molecule was tagged on the 5'end (that is, the 3'end of a messenger RNA transcript) with UMI and cell label indicating its cell of origin. Briefly, 10× beads that were then subject to second-strand cDNA synthesis, adaptor ligation, and universal amplification. Sequencing libraries were prepared using randomly interrupted whole-transcriptome amplification products to enrich the 3' end of the transcripts linked with the cell barcode and UMI. All the remaining procedures including the library construction were performed according to the standard manufacturer's protocol (CG000206 RevD). Sequencing libraries were quantified using a High Sensitivity DNA Chip (Agilent) on a Bioanalyzer 2100 and the Qubit High Sensitivity DNA Assay (Thermo Fisher Scientific). The libraries were sequenced on NovaSeq6000 (Illumina) using 2x150 chemistry.

Single-cell RNA-seq data processing

The raw scRNA-seq data were quantified using Cell Ranger (RRID: SCR_017344; version 7.0.0, 10x Genomics) with the GRCh38 as reference (16). The filtered_feature_bc_matrix files generated by Cell Ranger were filtered and analyzed via Seurat (RRID: SCR_016341; version 4.1.1) (17). Cells with detected transcripts fewer than 500, transcripts more than 50000 and

Downloaded from http://aacrjournals.org/clincancerres/article-pdf/doi/10.1158/1078-0432.CCR-25-3359/3748227/ccr-25-3359.pdf by guest on 01 April 2026

mitochondrial unique molecular identifier (UMI) percentage more than 30% were filtered out. DoubletFinder was used for each sequencing library to further remove potential doublets (18). After quality control, the count data were normalized, logarithmically transformed, and scaled by the *SCTransform* function. Batch effects were corrected by the *FindIntegrationAnchors* (with the parameter reduction= 'rpca') and *IntegrateData* functions. Dimensionality reduction was performed using the *RunPCA* and *RunUMAP* functions. Unsupervised clustering was conducted to get major cell clusters by the functions of *FindNeighbors* and *FindClusters* with the top 30 principal components and a resolution of 0.4. Canonical markers were used to annotate different cell types (Table S2).

CNV estimation

The CNV profiles of ductal cells were inferred via the inferCNV algorithm (RRID: SCR_021140) (19), with endothelial cells and fibroblasts serving as the normal reference. The CNVscore of each cell was calculated as the quadratic sum of CNV levels deviating from the normal level.

Signature genes identification

Differential expression analysis was performed using the *FindAllMarkers* function in the Seurat R package under different comparisons. The signatures of different ductal subclusters were defined based on the criteria of "avg_log2FC > 0.30, p_val_adj < 0.05", ribosomal and mitochondrial genes were excluded from signature genes. The signature genes of unipotent cells with higher plasticity were identified based on the criteria of "avg_log2FC > 0.5, p_val_adj < 0.05". To robustly define signature genes for HM tumor cells, patient-level analysis was applied by comparing HM versus PT cells within each patient. Genes upregulated in HM cells in more than 3 patients were identified as the HM signatures with "avg_log2FC > 0 and p_val_adj < 0.05".

Signature score and pathway score calculation

The signature and pathway scores of different genesets for the scRNA-seq data were calculated via AUCell (RRID: SCR_021327; version 1.16.0) (20). The *AUCell_buildRankings* function was applied to build gene expression rankings for each cell. Then the *AUCell_calcAUC* function was performed to calculate the scores of different genesets across cells.

The signature and pathway scores for bulkRNA-seq data from TCGA-PDAC cohort were calculated using the gene set variation analysis (GSVA) method (RRID: SCR_021058) (21). The log2sfCounts assay was used as the input and analyzed using the *gsva* function with the parameter kcdf = 'Gaussia'.

Pseudotime trajectory inference

Pseudotime analysis was performed on ductal cells using Monocle2 (RRID: SCR_016339; version 2.22.0) (22). The *newCellDataSet* function was used to generate the cds object. Genes that were highly variable and differentially expressed between different cell clusters were selected to infer the trajectory. The *reduceDimension* function was used for dimensionality reduction with the parameters reduction_method = 'DDRTree' and num_dim = 6. Cells were then arranged along the inferred trajectory using the *orderCells* function.

Developmental potential

CytoTRACE2 (version 1.1.0) (23) is a computational method for predicting cellular potency categories and absolute developmental potential from scRNA-seq data based on interpretable deep learning. The developmental potential was inferred using the *cytotrace2* function with

Downloaded from http://aacrjournals.org/clincancerres/article-pdf/doi/10.1158/1078-0432.CCR-25-3359/3748227/ccr-25-3359.pdf by guest on 01 April 2026

default parameters.

Survival analysis

The expression data and clinical information of 177 patients diagnosed with pancreatic adenocarcinoma were downloaded from The Cancer Genome Atlas (TCGA). To investigate the relationship between our results and metastasis, rigorously curated clinical follow-up information for the TCGA cohort, including the type, site, and date of new tumors, was obtained from a public article (24). The signature scores of each ductal subcluster were calculated using the GSVA method. Survival curves were fit by the *survfit* function of the R package survival (RRID: SCR_021137) (25) and visualized by the *ggsurvplot* function of the R package survminer (RRID: SCR_021094). The optimal cutoff point for patient grouping was estimated via the R package maxstat (26). Additionally, TCGA-PDAC patients were classified into the high metastatic risk group (highM) or the low metastatic risk group (lowM) based on metastatic sites and disease-free survival (DFS) duration. The highM group included patients with documented metastatic sites and a DFS of 365 days or less, while the lowM group comprised patients with documented metastatic sites and a DFS greater than 365 days.

Tissue microarray (TMA) construction

Two sets of TMAs were constructed for different research purposes. The first set of TMAs contained matched HMs and PTs from 22 metastatic PDAC patients. The second set of TMAs contained 67 PTs from high metastatic risk patients and 82 PTs from low metastatic risk patients.

Immunohistochemistry (IHC)

Immunohistochemical staining was performed on TMAs and formalin-fixed paraffin-embedded (FFPE) sections at a thickness of 4 μm. An intensity score of 0 to 3 was assigned for the intensity of tumor cells (0, none; 1, weak; 2, intermediate; 3, strong). A proportional score was given by the estimated proportion of positive tumor cells in percentage. To assess the average degree of staining within a tumor, multiple regions were analyzed, and at least 100 tumor cells were assessed. The cytoplasmic expression was assessed by H-Score system. The H-score was calculated as H-score = $\sum(I \times Pi)$, where I = intensity of staining and Pi = percentage of stained cells. We implemented immunohistochemistry for H2AFZ (Abcam, abs100991), LAG3 (RRID: AB_2133350; Proteintech, 16616-1-AP), PDCD1 (Servicebio, GB15338). DAPI (Life Technologies, 62247) was used as a nuclear counterstain. Images were obtained using the Zeiss Axioplan 2 Fluorescence microscope.

Knockdown of *H2AFZ* in PDAC cells

To achieve targeted gene knockdown of H2AFZ in PDAC cells, small interfering RNA (siRNA) oligonucleotides (Obio Technology, Shanghai, China) were transfected using Lipofectamine RNAiMAX (Thermo Fisher Scientific, Cat. no. 13778150) according to the manufacturer's protocol. The cells transfected with siRNA were collected after 48 hours for qRT-PCR to assess knockdown efficiency and for further assays. The specific siRNAs for H2AFZ were designed and synthesized by Genepharma (Shanghai, China); the sequences were shown as follows: siH2AFZ-1, CGUAUUCAUCGACACCUAA(dT)(dT); siH2AFZ-2, CGUCACUUGCAACUUGCUA(dT)(dT); the siRNA control (si-Ctrl) was non-homologous to any human genomic sequences. Lipofectamine® RNAiMAX reagent (Thermo Fisher Scientific, Cat. no. 13778030) was used to conduct siRNA transfection according to the manufacturer's protocols.

Quantitative real-time PCR (qRT-PCR)

Total RNA from PDAC cells was extracted using RNAiso Plus (Takara Bio, Cat. no. 9109) and

Downloaded from http://aacrjournals.org/clincancerres/article-pdf/doi/10.1158/1078-0432.CCR-25-3359/3748227/ccr-25-3359.pdf by guest on 01 April 2026

subsequently reverse transcribed into complementary DNA (cDNA) using the PrimeScript RT Reagent Kit (Takara Bio, Cat. no. RR037A). Following this, real-time PCR assays were conducted with TB Green Premix Ex Taq II (Takara Bio, Cat. no. RR820A) on an Applied Biosystems 7500 Real-Time PCR System (Thermo Fisher Scientific, USA), adhering to the recommended thermal cycling conditions (an initial cycle of 10 minutes at 95.0°C, followed by 40 cycles of 10 seconds at 95.0°C and 30 seconds at 60.0°C). Relative mRNA expression levels were normalized to the 18S RNA levels.

Cell culture

The human PDAC cell lines AsPC-1 (RRID: CVCL_0152), BxPC-3 (RRID: CVCL_0186), Capan-1 (RRID: CVCL_0237), Mia PaCa-2 (RRID: CVCL_0428), PANC-1 (RRID: CVCL_0480), Patu8988 (RRID: CVCL_1846), SW1990 (RRID: CVCL_1723) and the non-malignant pancreatic ductal epithelial cell line HPNE (RRID: CVCL C466) were all purchased from the Cell Bank of the Chinese Academy of Sciences and preserved at the Shanghai Cancer Institute, Ren Ji Hospital, School of Medicine, Shanghai Jiao Tong University. The mouse PDAC cell line KPC1199 was generated from KPC (*Pdx*^{cre}; LSL- *Kras*^{G12D}; LSL-*TP53*^{R172H}) mice as described previously (27-29) and generously provided by Prof. Jing Xue (State Key Laboratory of Oncogenes and Related Genes, Renji-Med X Clinical Stem Cell Research Center, Shanghai Cancer Institute, Renji Hospital, School of Medicine, Shanghai Jiao Tong University). Cells underwent high-density SNP typing for identity authentication and were verified to be *Mycoplasma*-free using MycoBlue Mycoplasma Detector (Vazyme, D101-01). All experiments shown were performed within a passage of <6 months from the acquisition of all cell lines. All cell lines were cultured in their recommended media as per American Type Culture Collection (ATCC) protocols, supplemented with 10% fetal bovine serum (FBS) and 1% streptomycin/penicillin (P/S). The cells were maintained in a humidified incubator under 5% CO_2 at 37°C.

Cell transwell migration assay

Transwell migration assay was performed using 6.5 mm chamber with 8 μm pores (Costar, Corning Incorporated, USA) housed in 24-well plates. Briefly, PDAC cells were resuspended in serum-free medium at a concentration of 4×10^4 cells per 200 μL and carefully loaded into the upper chamber. The lower compartment contained 700 μL of complete medium supplemented with 10% FBS. After 24 h of incubation, cells remaining on the upper membrane surface were removed using cotton swabs. Cells adherent to the lower membrane surface were subsequently washed with PBS, fixed with 4% paraformaldehyde for about 15 minutes, and stained with 0.1% crystal violet solution for 15 minutes for visualization. Quantitative analysis was performed by counting stained cells in three randomly selected fields per membrane using an inverted phase-contrast microscope (Zeiss AXIOVERT 200, Germany), with experiments performed in triplicate for each condition

Cell proliferation assay

Cell proliferation was assessed using the Cell Counting Kit-8 (CCK-8, MCE, Cat. no. HY-K0301) assay. Cells were seeded in 96-well plates at 2×10^3 cells/well (n=5 technical replicates) and allowed to adhere overnight. At 24 h intervals over a 5-day observation period, culture medium was replaced with fresh medium containing 10% (v/v) CCK-8 reagent, followed by 2 h incubation at 37°C under 5% CO_2. The absorbance values at 450 nm were measured using an automatic enzyme-linked immune detector (Bio-Rad Laboratories, Hercules, CA). Growth curves were generated from triplicate independent experiments. For the colony formation assay, cells were inoculated in 6-well plates at a density of 1500 cells per well and cultured for 12-14 days. Following this incubation,

Downloaded from http://aacrjournals.org/clincancerres/article-pdf/doi/10.1158/1078-0432.CCR-25-3359/3748227/ccr-25-3359.pdf by guest on 01 April 2026

colonies were fixed with 4% paraformaldehyde (Servicebio, Cat. no. G1101) for 30 minutes and subsequently stained with 0.1% crystal violet (Servicebio, Cat. no. G1014) for another 30 minutes. Photographs were taken, and colonies were counted under a microscope. Three independent experiments were performed for this assay as well.

Liver metastasis model for evaluating the function of *H2AFZ*

H2AFZ-targeting short hairpin RNAs (shRNAs) were designed and synthesized by GenePharma (Shanghai, China). To produce lentiviral particles, HEK293T (RRID: CVCL_0063) cells were co-transfected with the psPAX2 and pMD2.G packaging plasmids using Lipofectamine 2000 (Invitrogen, Cat#11668027), in accordance with established protocols. Target cells KPC1199 were then transduced with 1 × 10^6 infectious lentiviral units in the presence of 6 mg/mL polybrene (Sigma-Aldrich, Cat#H9268). Twenty-four hours post-transduction, selection was initiated by adding 5 μg/mL puromycin (Gibco, Cat#A1113802) to the culture medium. Stable puromycin-resistant clones were enriched over a 5-day selection period under continuous puromycin pressure (5 μg/mL). These selected cells were subsequently expanded through passaging, and the efficiency of *H2AFZ* knockdown was confirmed by both quantitative real-time PCR (qRT-PCR) and Western blot analysis.

C57BL/6J mice were used to establish a liver metastasis model of PDAC. Each mouse received an intrasplenic injection of 2 × 10^6 KPC1199 PDAC cells—both stably expressing luciferase—suspended in 25 μL of phosphate-buffered saline (PBS). Prior to injection, animals were anesthetized using isoflurane. Bioluminescent imaging was conducted on days 14 and 28 post-injection to track hepatic tumor burden: mice were first given an intraperitoneal dose of 150 mg D-luciferin (Promega, Madison, WI, USA; Cat# P1043), then anesthetized again with isoflurane and imaged using the IVIS Spectrum *in vivo* imaging system (PerkinElmer, Waltham, MA, USA). At the study endpoint (day 28), deeply anesthetized mice were humanely sacrificed via cervical dislocation. Their livers were harvested, fixed, and processed for histopathological analysis.

Liver metastasis model construction and immunotherapy treatment

All male C57BL/6 background mice were acquired from East China Normal University. Seven-week-old mice were used in this study. Mice were anaesthetized by inhalation anesthesia (2% isoflurane). And intrasplenic injections of KPC1199 cells were performed for the liver metastatic model, each mouse receiving 1 x 10^6 cells. After the injection, drugs (anti-PD1 and anti-LAG3) were intraperitoneally given every 3 days at a dose of 10 mg/kg. Five mice per group were randomly selected for bioluminescence imaging under 2% isoflurane inhalation anesthesia. Three weeks after the injection of KPC1199 cells, the mice were sacrificed and fixed with 4% paraformaldehyde.

Animals were housed in isolated ventilated cages barrier facility at Shanghai Jiao Tong University Laboratory Animal Center. Mice were maintained on a 12/12-hour light/dark cycle, 22-26 ℃ with sterile pellet food and water ad libitum. All animals received humane care according to the criteria outlined in the "Guide for the Care and Use of Laboratory Animals" prepared by the National Academy of Sciences and published by the National Institutes of Health. All manipulations were performed under approved protocol number 20141204 assigned by the Research Ethics Committee of East China Normal University.

Identification of treatment-induced genes by bulkRNA-seq

Tumor tissues from immunotherapy treated mice were subjected to bulk RNA sequencing. The raw reads of tumor tissues from immunotherapy treated mice were first processed using TrimGalore

Downloaded from http://aacrjournals.org/clincancerres/article-pdf/doi/10.1158/1078-0432.CCR-25-3359/3748227/ccr-25-3359.pdf by guest on 01 April 2026

(RRID: SCR_011847; version 0.6.7) (30) and the low-quality reads were removed to obtain the clean reads. The clean reads were mapped to the reference genome using STAR (RRID: SCR_004463; version 2.7.10) (31). The read counts and FPKM of each gene were calculated by featureCounts (RRID: SCR_012919). Principal component analysis (PCA) was performed to evaluate the biological replicates. Differentially expressed genes (DEGs) were identified by the DESeq2 (RRID: SCR_015687) R package ($p\_adj < 0.1$, $FoldChange > 0$ for DEGs_up and $FoldChange < 0$ for DEGs_down) (32). Based on the hypergeometric test, GO enrichment analysis of DEGs was performed to screen the significant enriched terms.

Statistical analysis

Statistical analyses used in this study included the t-test, Wilcoxon test, Fisher's exact test, among others, as described in the figure legends. The Kaplan-Meier method was applied for survival analysis.

Data availability

The raw sequencing data have been deposited into the Genomic Sequence Archive (Accession number: HRA008434). The public scRNA-seq data for healthy livers were collected from the Gene Expression Omnibus database (Accession number: GSE136103) (33). Additional data supporting the findings of this study are available from the corresponding author upon reasonable request.

Downloaded from http://aacrjournals.org/clincancerres/article-pdf/doi/10.1158/1078-0432.CCR-25-3359/3748227/ccr-25-3359.pdf by guest on 01 April 2026

Results

Single-cell transcriptomes of paired primary tumors and liver metastases in PDAC

To elucidate the cellular and molecular programs underlying PDAC hepatic metastasis, we enrolled 28 patients who underwent synchronous resection of primary tumors (PTs) and paired oligo-metastatic hepatic lesions (HMs). Single-cell RNA sequencing (scRNA-seq) was applied on 12 matched fresh-frozen PT and HM samples from six PDAC patients (Figure 1A; Table S1). PT and HM samples from the remaining 22 patients were used to construct tissue microarrays (TMAs) to validate key findings from the scRNA-seq data analysis. Additionally, TMAs constructed from primary tumors of 149 PDAC patients with follow-up information, along with bulkRNA-seq data from the TCGA-PDAC cohort, were leveraged to assess the prognostic significance and metastatic potential of the identified cell populations or genes of interest.

In total, 58,262 cells from 12 paired PT and HM samples were retained after stringent quality control. Upon data integration, unsupervised clustering and marker-based annotation (Table S2), 16 major cell types were identified including ductal cells, T cells, natural killer (NK) cells, B cells, hepatocytes, stellate cells, mast cells, plasma cells, neutrophils, myeloid cells (Mono/Macro/DC), fibroblasts, endothelial cells, proliferative cells, acinar cells, tuft cells and endocrine cells (Figure 1B and 1C). Acinar cells were exclusively detected in PTs while hepatocytes were present only in HMs, confirming the reliability of our cell type annotation. Ductal cells, fibroblasts, stellate cells and tuft cells were more abundant in PTs, while T cells and NK cells showed higher abundance in HMs ($P<0.05$, Figure 1D and 1E). These results indicate that tumor cells from PTs and HMs reside in different microenvironments, which may result in distinct tumor-TME crosstalk.

Cellular composition and functional analysis reveal increased tumor plasticity in metastatic PDAC

To interpret how malignant cells contribute to metastasis, we extracted 7150 ductal cells for subsequent analysis. Five ductal subclusters (C0-C4) were identified through unsupervised clustering (Figure 2A). Ductal cells of different subclusters represented distinct expression profiles, biological functions and cellular states (Figure 2B and 2C; Table S3 and S4). C3 exhibited a state resembling normal ductal cells based on the lowest copy number variation score (CNVscore) among all subclusters and its functions related to the normal pancreas, such as exocrine and pancreatic secretion (Figure 2C and 2D; Table S3 and S4). All subclusters except C3 were identified as malignant based on their increased CNV burden and functional annotations (Figure 2C). C0 was associated with cell junction assembly and the cell surface receptor signaling pathway. C1 displayed biological functions related to antigen processing and presentation, and T cell activation. C2 exhibited stronger oxidative phosphorylation (OXPHOS), DNA repair activity, and the MYC signaling pathway. C4 showed functions related to cytoskeleton and cell migration, but the number of cells in C4 was too low for a robust analysis.

The PTs and HMs exhibited distinct cellular compositions. HMs contained more C2 and C0 subclusters, while PTs contained more C1, C3 and C4 subclusters. When analyzing the cellular compositions of ductal subclusters within each patient, we observed that C2 was more prevalent in HMs in 5 out of 6 patients (Figure 2E). Besides, we employed a public dataset containing 3 additional pairs of PT and HM samples and observed the same trend of increased C2 abundance in HMs in 2 out of 3 patients (Figure S1A and S1B). Integrating our private dataset

Downloaded from http://aacrjournals.org/clincancerres/article-pdf/doi/10.1158/1078-0432.CCR-25-3359/3748227/ccr-25-3359.pdf by guest on 01 April 2026

with this public dataset, 7 out of 9 metastatic patients exhibited a trend of increased C2 tumor cells in hepatic metastases (Figure S1B). In addition, C2 formed a separate developmental branch compared to other subclusters (Figure 2F). We then evaluated the clinical relevance of each subcluster in the TCGA-PDAC cohort. Notably, C2 was the only subcluster that negatively associated with both overall survival (OS) and disease-free survival (DFS) ($P < 0.01$, Figure 2G). Furthermore, when looking into non-metastatic tumors which later developed hepatic metastases during follow-up, the primary tumors at high risk of hepatic metastasis (highHM, DFS $\leqslant$ 365 days) exhibited significantly higher C2 signature scores than those at low risk of hepatic metastasis (lowHM, DFS > 365 days) ($P = 0.026$, Figure 2H).

Partial epithelial–mesenchymal transition (pEMT), rather than complete EMT (cEMT), has been reported to play a more vital role in tumor progression and metastasis. A recent study employed lineage tracing to track and classify the EMT process into 6 states including complete epithelial, hybrid EMT (H1~4) and complete mesenchymal states (34). We estimated the EMT state scores across tumor cells and found that C2 showed higher hybrid EMT scores than other tumor subclusters (Figure 2I and S1C). Given that the 6 EMT states were identified in mouse models, we performed a parallel analysis using genesets derived from a human pan-cancer study (35). Similar to the above results, C2 exhibited higher pEMT scores compared to other subclusters, while having lower mesenchymal scores (Figure 2J and S1D). pEMT or hybrid EMT manifests a transitional state of higher cell plasticity. To quantify this property, we used CytoTRACE2 (23) to calculate a cellular potency score, where higher values indicate a less differentiated, more plastic state. Our analysis confirmed that C2 possessed a significantly higher potency score ($P < 0.001$, Figure 2K and 2L). Interestingly, this plastic state appears to be associated with metastatic progression. When comparing tumor cells from different sites, those in HMs exhibited markedly higher potency scores than cells in PTs ($P < 0.001$, Figure 2L).

In summary, these results collectively indicate that C2 is associated with higher hepatic metastasis risk and worse prognosis. C2 tumor cells reprogram the expression profiles and transit into a plastic state to facilitate hepatic metastasis.

Identification of *H2AFZ* as a major driver of malignant cell proliferation and hepatic metastasis

To robustly identify the potential driver genes of the C2 subpopulation, we intersected the signature genes of C2, HM and unipotent tumor cells with higher plasticity (Figure 3A; Table S5). This analysis yielded six common genes, among which *H2AFZ* and *PFN1* showed significant prognostic value for both OS and DFS (Figure 3B and S1E). Given that the role of *PFN1* in tumorigenesis is contentious and highly context-specific (36,37), we focused our subsequent investigation on *H2AFZ*, a histone variant consistently implicated in promoting tumor cell proliferation and metastasis in multiple cancers (38,39). However, the role of *H2AFZ* in PDAC metastasis remains largely unexplored.

The strong association between *H2AFZ* expression and the C2 subpopulation was further confirmed in the independent TCGA-PDAC cohort ($R = 0.68$, $P < 2.2e{-}16$; Figure 3C). To directly link *H2AFZ* to the metastatic phenotype, we performed immunohistochemistry (IHC) on paired primary and metastatic tumors from an additional 22 patients. This confirmed that H2AFZ protein levels were significantly elevated in metastatic lesions (Figure 3D). Moreover, analysis of 149 PDAC primary tumors showed markedly higher H2AFZ levels in the highM

Downloaded from http://aacrjournals.org/clincancerres/article-pdf/doi/10.1158/1078-0432.CCR-25-3359/3748227/ccr-25-3359.pdf by guest on 01 April 2026

group than in the lowM group (Figure 3E), further supporting its association with metastatic potential. Importantly, elevated H2AFZ expression was again found to correlate with poor prognosis in our private dataset, showing negative associations with both OS and DFS (Figure 3F).

Given *H2AFZ*'s reported function in cell proliferation (38,40), we next examined its relationship with proliferative activity in PDAC. Correlation analysis in the TCGA-PDAC cohort showed that *H2AFZ* expression positively correlated with the cell cycle score (Figure 3G). In our metastatic PDAC samples, HM samples with elevated H2AFZ expression also exhibited increased MKI67 levels, a well-known proliferation marker (Figure 3H). Functional experiments demonstrated that knockdown of *H2AFZ* in two human PDAC cell lines, Patu8988 and SW1990, significantly reduced colony formation and impaired proliferative capacity of PDAC tumor cells (Figure 3I and 3J).

Beyond proliferation, we explored *H2AFZ*'s role in tumor cell migration, a critical step in metastatic dissemination. Knockdown of *H2AFZ* substantially suppressed tumor migratory ability in the transwell migration assay (Figure 3K). We also performed *in vivo* experiments to evaluate the impact of *H2AFZ* on liver metastasis using mouse metastatic models. The results showed that *H2AFZ* knockdown significantly repressed tumor growth in the liver compared with the control group (Figure 3L-N). Taken together, these findings indicate that *H2AFZ* plays a vital role during hepatic metastasis, potentially by regulating both tumor cell proliferation and migratory capacity.

PDAC metastasis remodels an immunosuppressive hepatic microenvironment

To understand the immune microenvironment of hepatic metastases (HMs), we collected public scRNA-seq data for healthy liver samples (HLs) (33) and compared the myeloid and T cell compositions between HMs and HLs (Figure S2A-F). Clustering analysis of 3894 myeloid cells identified 8 myeloid subclusters: Mye0 CD16+ monocytes, Mye1 CD14+ monocytes, Mye2 SPP1+ macrophages, Mye3 C1QC+ macrophages, Mye4 CLEC9A+ cDC1s, Mye5 CLEC10A+ cDC2s, Mye6 LAMP3+ cDCs and Mye7 LILRA4+ plasmacytoid dendritic cells (pDCs) (Figure 4A, 4B). SPP1+ and C1QC+ macrophages exhibited higher proportions in HMs than HLs (Figure 4C and S2C). Those two myeloid subclusters have been associated with tumor progression in multiple malignancies (41). We scored all myeloid cells with signature genes of previously reported M1 and M2 macrophages (42), which represent the pro-inflammatory and the anti-inflammatory states, respectively (Table S6) (43,44). M1 scores were highest in CD14+ monocytes and LAMP3+cDCs, whereas M2 scores were highest in C1QC+ macrophages and SPP1+ macrophages (Figure 4D). Pseudotime trajectory analysis using Monocle2 revealed that monocytes differentiated along two distinct branches, one leading to SPP1+ macrophages and the other to C1QC+ macrophages (Figure 4E). These results suggest that myeloid cells exhibited a shift from pro-inflammatory toward anti-inflammatory states, raising the possibility that macrophages in hepatic metastases may suppress immune activity and facilitate tumor growth, although further investigation is needed.

T cells also constitute a critical part of the TME in metastatic PDAC. To characterize them, we conducted clustering analysis on 26858 T cells in metastatic PDAC. Three CD4+ T cell subclusters (T6-T8), five CD8+ T cell subclusters (T0-T4), and one CD4-CD8- NK-like T (NKT) cell subcluster (T5) were identified (Figure 4F-G). Among them, T6 and T7 were recognized as naïve T cells due to the low expression of genes related to helper T cell functions

Downloaded from http://aacrjournals.org/clincancerres/article-pdf/doi/10.1158/1078-0432.CCR-25-3359/3748227/ccr-25-3359.pdf by guest on 01 April 2026

and relatively high expression of naïve T cell related genes such as *LEF1* and *CCR7* (Figure 4G and S2D). T8 was identified as regulatory T cells based on the expression of *FOXP3*, *CTLA4* and other relevant markers. T0 and T1 were identified as CD8+ cytotoxic effector T cells, with *CCL4* highly expressed in T0 and *AOAH* highly expressed in T1. T2 exhibited higher expression of genes related to the interferon signaling pathway, suggesting a response to interferons. T3 represented T cells in an exhausted state, characterized by the expression of *PDCD1* and *HAVCR2*. T4 was classified as mucosal-associated invariant T cells (MAITs), an innate-like T cell subset that is overabundant in the liver (45). T5 was identified as NKT cells due to high expression of both T cell and NK cell markers. HMs exhibited more Treg and Tex cells compared to HLs, suggesting a more immunosuppressive state in hepatic metastatic lesions than in uncolonized livers (Figure 4H and S2F).

Next, we explored the cell–cell communications between tumor cells and immune cells in the hepatic metastases using CellChat (46). We observed the strongest MDK-SDC2 interaction between HM-promoting C2 tumor cells and suppressive SPP1+ macrophages compared to other tumor subclusters (Figure 4I). Notably, the MDK–SDC2 interaction has previously been associated with M2 macrophages (47), which are known to support an immunosuppressive TME. The interaction between C2 tumor cells and exhausted T cells (T3) was probably mediated by LAMA3-(ITGA1+ITGB1) (Figure 4I). In turn, SPP1+ macrophages interacted with C2 tumor cells through multiple ligand–receptor pairs, including LGALS9-CD44, RETN-CAP1, and SPP1-CD44, several of which have been implicated in promoting tumor cell stemness, invasion, and metastasis, thereby reinforcing the pro-tumoral microenvironment in HMs (Figure 4J) (48,49). Together, these findings highlight an immune-suppressive TME in HMs relative to unaffected livers, characterized by increased abundances of M2-like SPP1+ macrophages, C1QC+ macrophages, regulatory T cells, and exhausted T cells. We also identified potential interactions that may mediate this suppressive microenvironment.

Effectiveness of anti-PD1 combined with anti-LAG3 for PDAC hepatic metastases

Current treatment strategies have shown considerably limited efficacy in PDAC (5). The above analysis revealed that pancreatic tumor cells are capable of remodeling the liver TME, leading to an immuno-suppressive milieu that, in turn, promotes tumor cell growth. Targeting this immuno-suppressive TME may serve as an effective treatment strategy for PDAC. Therefore, we analyzed the expression of immune-suppressing and immune-activating genes in T cells derived from PTs and HMs (Figure 5A). Notably, exhausted T cells (T3) in HMs exhibited elevated expression of immune checkpoint genes *PDCD1* and *LAG3* (Figure 5A). Elevated expression of PD1 and LAG*3* in HMs compared with PTs was also confirmed via IHC in another 22 PDAC patients (Figure 5B and 5C). These results suggest a more pronounced state of T cell exhaustion in metastatic liver lesions than in primary tumors.

Beyond the well-known suppressive receptor *PDCD1*, *LAG3* attracted our attention as a novel immune checkpoint molecule expressed on T cells, whose ligands *FGL1* and *CLEC4G* can suppress T cell responses (50). Interestingly, *FGL1* is produced by hepatocytes especially when injured and *CLEC4G* is highly expressed by liver sinusoidal endothelial cells (LESCs), raising the possibility that *LAG3* inhibition could be a relevant therapeutic strategy for patients with hepatic metastasis. Our scRNA-seq data confirmed this exclusive pattern of expression in hepatocytes and LSECs in HMs (Figure S3A).

Given the concurrent upregulation of both *PDCD1* and *LAG3*, we hypothesized that dual

Downloaded from http://aacrjournals.org/clincancerres/article-pdf/doi/10.1158/1078-0432.CCR-25-3359/3748227/ccr-25-3359.pdf by guest on 01 April 2026

blockade of these inhibitory receptors might enhance therapeutic efficacy. Consequently, we administered anti-PD1 alone (aPD1), anti-LAG3 alone (aLAG3), or a combination of anti-PD1 and anti-LAG3 (aPD1+aLAG3) to metastatic mouse models to evaluate their therapeutic effects on liver metastases (Figure 5D, 5E and 5F). Compared with the untreated control, aPD1 treatment delayed the growth of metastatic tumors, while aLAG3 mildly repressed the growth of metastatic tumors. Strikingly, the combination therapy significantly outperformed either monotherapy, demonstrating enhanced anti-tumor efficacy (Figure 5D and 5E).

To elucidate the underlying mechanisms of this improved therapeutic response, we performed bulkRNA-seq on tumor tissues harvested from metastatic mouse models following treatment. Principal component analysis revealed a clear transcriptional separation between the treated and control groups, underscoring the substantial impact of immunotherapy on tumor gene expression (Figure 5G). Compared to the control group, the aPD1 + aLAG3 group exhibited upregulation of 460 genes and downregulation of 517 genes. Of these, only 94 upregulated and 181 downregulated genes overlapped with those affected in the aPD1 monotherapy group, suggesting that the combination therapy induces a broader and distinct transcriptional reprogramming (Figure 5H and Figure S3B). We further conducted Gene Ontology (GO) enrichment analysis to explore the functional changes at the pathway level. The aPD1 group was associated with immune-related pathways, such as leukocyte cell-cell adhesion, regulation of T cell activation and cell chemotaxis, consistent with the effect of aPD1 therapy in reinvigorating the anti-tumor immunity (Figure 5I; Table S7 and S8). Compared to aPD1 alone, the combination treatment further enhanced pathways associated with chemokine responses and myeloid cell migration (Figure 5I, 5J and S3C). We speculate that aLAG3 therapy may relieve the immune suppression caused by the immune-privileged phenotype of the liver, thereby enhancing the therapeutic efficacy when combined with aPD1 therapy. Moreover, the dual blockade decreased the activity of pathways involved in epithelial cell morphogenesis and negative regulation of lymphocyte differentiation (Figure S3D; Table S7 and S8). In summary, we observed T cell state heterogeneity within and across organs and primarily explored the possibility of treating PDAC using a novel combination strategy of aPD1 and aLAG3.

Discussion

Metastasis is a highly dynamic, multistep biological process, during which tumor cells disseminate from the primary site, colonize distant organs, and adapt to new microenvironments. In this study, we applied scRNA-seq, bulkRNA-seq, IHC, and experimental validation to PDAC patients and murine models, revealing a malignant cellular subpopulation and immunosuppressive microenvironment closely associated with PDAC liver metastasis (Figure 6). Based on the characteristics of the metastatic microenvironment, we proposed a novel combination strategy targeting both PD1 and LAG3, which significantly inhibited tumor growth in mouse models of metastasis. These findings highlight the heterogeneity of malignant cells and the tumor microenvironment in metastatic PDAC, and propose a new exploratory combination therapy approach that warrants further investigation.

Tumor cells, as the “seeds” of metastasis, are undoubtedly the most critical and central cell population of interest in studies of metastatic progression. However, focusing on these cells is particularly challenging, as analyses based solely on primary tumors or unpaired samples cannot fully capture the post-metastatic state and are prone to substantial noise arising from

Downloaded from http://aacrjournals.org/clincancerres/article-pdf/doi/10.1158/1078-0432.CCR-25-3359/3748227/ccr-25-3359.pdf by guest on 01 April 2026

inter-patient heterogeneity. Previous studies by Lee et al. and Lin et al. applied scRNA-seq to unpaired PTs and HMs, offering insights into TME remodeling (12,13). However, the tumor cells in these studies are not directly comparable, as they originate from different patients and the heterogeneity of tumor cells is known to be substantial. Zhang et al. addressed this limitation by performing scRNA-seq on paired PT and HM samples, identifying subpopulations associated with metastatic TME formation (14). Nevertheless, their study was constrained by only three pairs of samples, making the analysis highly sensitive—any difference in a single patient could substantially affect the conclusions. To overcome these limitations, we expanded our cohort of paired samples and incorporated these publicly available datasets to enable more robust intra-patient comparisons. Comparative analysis of paired PTs and HMs within individual patients allows better control of inter-patient variability and facilitates the identification of more conserved metastatic signals. Although our dataset is still limited in size due to the difficulty of obtaining simultaneously resected paired samples, the results have been validated from multiple perspectives. Larger cohorts and more advanced technologies, such as single-cell resolution spatial omics, will be necessary to further elucidate the roles of tumor cells and uncover more subtle cues in PDAC liver metastasis.

Previous studies have demonstrated that the metastatic potential of different tumor cells differ, with some tumor cell lines exhibiting inherently higher metastatic potential (34,51). Here in our work, we identified a tumor subpopulation, C2, characterized by a less differentiated, highly proliferative phenotype and associated with enhanced metastatic potential. This phenotype appears to be largely driven by *H2AFZ*, a histone variant previously implicated in tumor growth and progression across multiple malignancies, including hepatocellular carcinoma and canine melanoma (52,53). In hepatocellular carcinoma, Dong et al. revealed that *H2AFZ* overexpression is regulated by *TP53* mutation (52), which is one of the predominant mutations in PDAC. This prompted us to explore the relationship between *H2AFZ* and the most common genomic alterations in PDAC. Using genomic and transcriptomic data from the TCGA_PDAC cohort, we observed an association between *H2AFZ* expression, and *KRAS* and *TP53* expression, while *SMAD4* and *CDKN2A* did not affect *H2AFZ* expression (Figure S4A). In addition, *H2AFZ* appeared to be associated with *KRAS* mutant dosage, which is a risk factor involved in PDAC progression (54). Patients with gain/amplification and higher variant allele frequency at the *KRAS* locus exhibited higher *H2AFZ* expression (Figure S4B and S4C). However, the mechanisms by which these genomic alterations regulate *H2AFZ* expression remain to be elucidated and warrant further investigation.

The exhausted T cells in immunosuppressive HMs exhibited elevated expression of both *PDCD1* and *LAG3*. Immune checkpoint inhibitors targeting these two genes led to enhanced effects in our study. Similar to our results, this combination strategy has also shown promising results in advanced melanoma (55). The comparison of pre-treatment and post-treatment transcriptomes showed that upregulated expression of immune-related genes may contribute to the augmented effects. Further mechanistic investigations and clinical trials are necessary and valuable to determine whether this therapy is effective and safe for treating metastatic PDAC in human.

Although our study provides new insights into metastatic PDAC, several points should be considered when interpreting our findings. First, although we incorporated publicly available datasets and performed multi-faceted validation to strengthen the robustness of our findings,

Downloaded from http://aacrjournals.org/clincancerres/article-pdf/doi/10.1158/1078-0432.CCR-25-3359/3748227/ccr-25-3359.pdf by guest on 01 April 2026

the number of patients included in our cohort remains relatively limited. Future studies involving larger, independent cohorts and more advanced spatial and multi-omics technologies will be necessary to further substantiate and extend our conclusions. Second, our analyses were primarily based on patients with oligo-hepatic metastases. The biological features of these cases may differ from those of patients with multiple liver metastatic lesions or multi-organ metastases, and therefore caution is warranted when generalizing our findings to broader metastatic settings. Third, in the final part of this study, we evaluated the efficacy of combined immunotherapy in mouse models and observed encouraging therapeutic responses. Nevertheless, given the intrinsic physiological and immunological differences between murine models and humans, the safety and efficacy of such combination strategies require more systematic and rigorous evaluation in future preclinical and clinical studies.

In summary, our work collectively advances the understanding of PDAC liver metastasis at the single-cell level, and offers new insights that may improve the treatment responses for PDAC patients.

Acknowledgments

This study was supported by grants from the National Natural Science Foundation of China (32300555 to P. Lin, 32470707 to H. Li, 82473029 to J.Y. Yang, 82472917 to Y.W. Sun) and Shanghai Sailing Program (22YF1458000 to P. Lin).

Contributions

Yongwei Sun, Hong Li, Ping Lin and Yingbin Liu designed the study and were the co-corresponding authors. Jianyu Yang and Wanhong Chen prepared the manuscript. Wanhong Chen conducted omics data analysis in this study and assisted in interpreting the results. Jianyu Yang designed and performed the experiments and interpreted the experimental results. Zonghao Duan, Minwei Yang, Lingye Tao, Yanmiao Huo, Wei Liu, Junfeng Zhang, and Linli Yao helped conduct experiments. All authors read and approved the final manuscript.

Ethics Statement

The study was approved by the Research Ethics Committee of Renji Hospital, School of Medicine, Shanghai Jiao Tong University (LY2024-064-B) and informed consent was obtained from each participant.

Downloaded from http://aacrjournals.org/clincancerres/article-pdf/doi/10.1158/1078-0432.CCR-25-3359/3748227/ccr-25-3359.pdf by guest on 01 April 2026

References

1. Siegel RL, Miller KD, Wagle NS, Jemal A. Cancer statistics, 2023. *CA: A Cancer Journal for Clinicians* 2023;**73**(1):17-48 doi 10.3322/caac.21763.
2. Nichetti F, Rota S, Ambrosini P, Pircher C, Gusmaroli E, Droz Dit Busset M*, et al.* NALIRIFOX, FOLFIRINOX, and Gemcitabine With Nab-Paclitaxel as First-Line Chemotherapy for Metastatic Pancreatic Cancer: A Systematic Review and Meta-Analysis. *JAMA Netw Open* 2024;**7**(1):e2350756 doi 10.1001/jamanetworkopen.2023.50756.
3. Wainberg ZA, Melisi D, Macarulla T, Pazo Cid R, Chandana SR, De La Fouchardière C*, et al.* NALIRIFOX versus nab-paclitaxel and gemcitabine in treatment-naive patients with metastatic pancreatic ductal adenocarcinoma (NAPOLI 3): a randomised, open-label, phase 3 trial. *Lancet* 2023;**402**(10409):1272-81 doi 10.1016/S0140-6736(23)01366-1.
4. Strickler JH, Satake H, George TJ, Yaeger R, Hollebecque A, Garrido-Laguna I*, et al.* Sotorasib in KRAS p.G12C-Mutated Advanced Pancreatic Cancer. *N Engl J Med* 2022;**388**(1):33-43 doi 10.1056/NEJMoa2208470.
5. O'Reilly EM, Oh D-Y, Dhani N, Renouf DJ, Lee MA, Sun W*, et al.* Durvalumab With or Without Tremelimumab for Patients With Metastatic Pancreatic Ductal Adenocarcinoma: A Phase 2 Randomized Clinical Trial. *JAMA Oncol* 2019;**5**(10):1431-8 doi 10.1001/jamaoncol.2019.1588.
6. Ozaki K, Higuchi S, Kimura H, Gabata T. Liver Metastases: Correlation between Imaging Features and Pathomolecular Environments. *Radiographics* 2022;**42**(7):1994-2013 doi 10.1148/rg.220056.
7. Groot VP, Gemenetzis G, Blair AB, Ding D, Javed AA, Burkhart RA*, et al.* Implications of the Pattern of Disease Recurrence on Survival Following Pancreatectomy for Pancreatic Ductal Adenocarcinoma. *Annals of Surgical Oncology* 2018;**25**(8):2475-83 doi 10.1245/s10434-018-6558-7.
8. Yang J, Lin P, Yang M, Liu W, Fu X, Liu D*, et al.* Integrated genomic and transcriptomic analysis reveals unique characteristics of hepatic metastases and pro-metastatic role of complement C1q in pancreatic ductal adenocarcinoma. *Genome Biol* 2021;**22**(1):4 doi 10.1186/s13059-020-02222-w.
9. Che L-H, Liu J-W, Huo J-P, Luo R, Xu R-M, He C*, et al.* A single-cell atlas of liver metastases of colorectal cancer reveals reprogramming of the tumor microenvironment in response to preoperative chemotherapy. *Cell Discovery* 2021;**7**(1):80 doi 10.1038/s41421-021-00312-y.
10. Puram SV, Tirosh I, Parikh AS, Patel AP, Yizhak K, Gillespie S*, et al.* Single-Cell Transcriptomic Analysis of Primary and Metastatic Tumor Ecosystems in Head and Neck Cancer. *Cell* 2017;**171**(7) doi 10.1016/j.cell.2017.10.044.
11. Zhang Y, You W-H, Li X, Wang P, Sha B, Liang Y*, et al.* Single-cell RNA-seq reveals transcriptional landscape and intratumor heterogenicity in gallbladder cancer liver metastasis microenvironment. *Ann Transl Med* 2021;**9**(10):889 doi 10.21037/atm-21-2227.
12. Lin W, Noel P, Borazanci EH, Lee J, Amini A, Han IW*, et al.* Single-cell transcriptome analysis of tumor and stromal compartments of pancreatic ductal adenocarcinoma primary tumors and metastatic lesions. *Genome Medicine* 2020;**12**(1) doi 10.1186/s13073-020-00776-9.

Downloaded from http://aacrjournals.org/clincancerres/article-pdf/doi/10.1158/1078-0432.CCR-25-3359/3748227/ccr-25-3359.pdf by guest on 01 April 2026

13. Lee JJ, Bernard V, Semaan A, Monberg ME, Huang J, Stephens BM*, et al.* Elucidation of Tumor-Stromal Heterogeneity and the Ligand-Receptor Interactome by Single-Cell Transcriptomics in Real-world Pancreatic Cancer Biopsies. *Clin Cancer Res* 2021;**27**(21):5912-21 doi 10.1158/1078-0432.CCR-20-3925.
14. Zhang S, Fang W, Zhou S, Zhu D, Chen R, Gao X*, et al.* Single cell transcriptomic analyses implicate an immunosuppressive tumor microenvironment in pancreatic cancer liver metastasis. *Nat Commun* 2023;**14**(1):5123 doi 10.1038/s41467-023-40727-7.
15. Yang J, Zhang J, Lui W, Huo Y, Fu X, Yang M*, et al.* Patients with hepatic oligometastatic pancreatic body/tail ductal adenocarcinoma may benefit from synchronous resection. *HPB (Oxford)* 2019;**22**(1) doi 10.1016/j.hpb.2019.05.015.
16. Zheng GXY, Terry JM, Belgrader P, Ryvkin P, Bent ZW, Wilson R*, et al.* Massively parallel digital transcriptional profiling of single cells. *Nature Communications* 2017;**8**:14049 doi 10.1038/ncomms14049.
17. Hao Y, Hao S, Andersen-Nissen E, Mauck WM, Zheng S, Butler A*, et al.* Integrated analysis of multimodal single-cell data. *Cell* 2021;**184**(13) doi 10.1016/j.cell.2021.04.048.
18. McGinnis CS, Murrow LM, Gartner ZJ. DoubletFinder: Doublet Detection in Single-Cell RNA Sequencing Data Using Artificial Nearest Neighbors. *Cell Syst* 2019;**8**(4) doi 10.1016/j.cels.2019.03.003.
19. Patel AP, Tirosh I, Trombetta JJ, Shalek AK, Gillespie SM, Wakimoto H*, et al.* Single-cell RNA-seq highlights intratumoral heterogeneity in primary glioblastoma. *Science (New York, NY)* 2014;**344**(6190):1396-401 doi 10.1126/science.1254257.
20. Aibar S, González-Blas CB, Moerman T, Huynh-Thu VA, Imrichova H, Hulselmans G*, et al.* SCENIC: single-cell regulatory network inference and clustering. *Nature methods* 2017;**14**(11):1083-6.
21. Hänzelmann S, Castelo R, Guinney J. GSVA: gene set variation analysis for microarray and RNA-seq data. *BMC Bioinformatics* 2013;**14**:7 doi 10.1186/1471-2105-14-7.
22. Trapnell C, Cacchiarelli D, Grimsby J, Pokharel P, Li S, Morse M*, et al.* The dynamics and regulators of cell fate decisions are revealed by pseudotemporal ordering of single cells. *Nature Biotechnology* 2014;**32**(4):381-6 doi 10.1038/nbt.2859.
23. Kang M, Armenteros JJA, Gulati GS, Gleyzer R, Avagyan S, Brown EL*, et al.* Mapping single-cell developmental potential in health and disease with interpretable deep learning. 2024:2024.03. 19.585637.
24. Liu J, Lichtenberg T, Hoadley KA, Poisson LM, Lazar AJ, Cherniack AD*, et al.* An Integrated TCGA Pan-Cancer Clinical Data Resource to Drive High-Quality Survival Outcome Analytics. *Cell* 2018;**173**(2):400-16.e11 doi 10.1016/j.cell.2018.02.052.
25. Therneau TM, Lumley T. Package 'survival'. *R Top Doc* 2015;**128**(10):28-33.
26. Hothorn T, Lausen B. Maximally selected rank statistics in R. *R News* 2002;**2**(1):3-5.
27. Niu N, Shen X, Zhang L, Chen Y, Lu P, Yang W*, et al.* Tumor Cell-Intrinsic SETD2 Deficiency Reprograms Neutrophils to Foster Immune Escape in Pancreatic Tumorigenesis. *Advanced Science (Weinheim, Baden-Wurttemberg, Germany)* 2022;**10**(2):e2202937 doi 10.1002/advs.202202937.
28. Niu N, Lu P, Yang Y, He R, Zhang L, Shi J*, et al.* Loss of Setd2 promotes Kras-induced acinar-to-ductal metaplasia and epithelia-mesenchymal transition during pancreatic carcinogenesis. *Gut* 2019;**69**(4):715-26 doi 10.1136/gutjnl-2019-318362.

Downloaded from http://aacrjournals.org/clincancerres/article-pdf/doi/10.1158/1078-0432.CCR-25-3359/3748227/ccr-25-3359.pdf by guest on 01 April 2026

29. He W, Wu J, Shi J, Huo Y-M, Dai W, Geng J*, et al.* IL22RA1/STAT3 Signaling Promotes Stemness and Tumorigenicity in Pancreatic Cancer. *Cancer Research* 2018;**78**(12):3293-305 doi 10.1158/0008-5472.CAN-17-3131.
30. Krueger F. Trim Galore!: A wrapper around Cutadapt and FastQC to consistently apply adapter and quality trimming to FastQ files, with extra functionality for RRBS data. *Babraham Institute* 2015.
31. Dobin A, Gingeras TR. Mapping RNA‐seq reads with STAR. *Current protocols in bioinformatics* 2015;**51**(1):11.4. 1-.4. 9.
32. Love MI, Huber W, Anders S. Moderated estimation of fold change and dispersion for RNA-seq data with DESeq2. *Genome Biology* 2014;**15**(12):550.
33. Ramachandran P, Dobie R, Wilson-Kanamori JR, Dora EF, Henderson BEP, Luu NT*, et al.* Resolving the fibrotic niche of human liver cirrhosis at single-cell level. *Nature* 2019;**575**(7783):512-8 doi 10.1038/s41586-019-1631-3.
34. Simeonov KP, Byrns CN, Clark ML, Norgard RJ, Martin B, Stanger BZ*, et al.* Single-cell lineage tracing of metastatic cancer reveals selection of hybrid EMT states. *Cancer Cell* 2021;**39**(8):1150-62 e9 doi 10.1016/j.ccell.2021.05.005.
35. Barkley D, Moncada R, Pour M, Liberman DA, Dryg I, Werba G*, et al.* Cancer cell states recur across tumor types and form specific interactions with the tumor microenvironment. *Nat Genet* 2022;**54**(8):1192-201 doi 10.1038/s41588-022-01141-9.
36. Gau D, Chawla P, Xu K, Welling N, Antonello J, Consoli C*, et al.* Small molecule intervention of actin-binding protein profilin1 reduces tumor angiogenesis in renal cell carcinoma. *BioRxiv : the Preprint Server For Biology* 2025 doi 10.1101/2025.07.18.665115.
37. Yao W, Ji S, Qin Y, Yang J, Xu J, Zhang B*, et al.* Profilin-1 suppresses tumorigenicity in pancreatic cancer through regulation of the SIRT3-HIF1α axis. *Molecular Cancer* 2014;**13**:187 doi 10.1186/1476-4598-13-187.
38. Yang HD, Kim P-J, Eun JW, Shen Q, Kim HS, Shin WC*, et al.* Oncogenic potential of histone-variant H2A.Z.1 and its regulatory role in cell cycle and epithelial-mesenchymal transition in liver cancer. *Oncotarget* 2016;**7**(10):11412-23 doi 10.18632/oncotarget.7194.
39. Qiu L, Zeng X, Han J. Histone variant H2A.Z facilitates DNA replication. *Science China Life Sciences* 2020;**63**(5):788-90 doi 10.1007/s11427-020-1673-1.
40. Svotelis A, Gévry N, Grondin G, Gaudreau L. H2A.Z overexpression promotes cellular proliferation of breast cancer cells. *Cell Cycle* 2010;**9**(2):364-70.
41. Li X, Zhang Q, Chen G, Luo D. Multi-Omics Analysis Showed the Clinical Value of Gene Signatures of C1QC+ and SPP1+ TAMs in Cervical Cancer. *Front Immunol* 2021;**12**:694801 doi 10.3389/fimmu.2021.694801.
42. Cheng S, Li Z, Gao R, Xing B, Gao Y, Yang Y*, et al.* A pan-cancer single-cell transcriptional atlas of tumor infiltrating myeloid cells. *Cell* 2021;**184**(3):792-809 e23 doi 10.1016/j.cell.2021.01.010.
43. Mantovani A, Sozzani S, Locati M, Allavena P, Sica A. Macrophage polarization: tumor-associated macrophages as a paradigm for polarized M2 mononuclear phagocytes. *Trends In Immunology* 2002;**23**(11):549-55.
44. Hu H, Hang J-J, Han T, Zhuo M, Jiao F, Wang L-W. The M2 phenotype of tumor-associated macrophages in the stroma confers a poor prognosis in pancreatic cancer. *Tumour Biol* 2016;**37**(7):8657-64 doi 10.1007/s13277-015-4741-z.

Downloaded from http://aacrjournals.org/clincancerres/article-pdf/doi/10.1158/1078-0432.CCR-25-3359/3748227/ccr-25-3359.pdf by guest on 01 April 2026

45. Provine NM, Klenerman P. MAIT Cells in Health and Disease. *Annu Rev Immunol* 2020;**38**:203-28 doi 10.1146/annurev-immunol-080719-015428.

46. Jin S, Guerrero-Juarez CF, Zhang L, Chang I, Ramos R, Kuan CH*, et al.* Inference and analysis of cell-cell communication using CellChat. *Nat Commun* 2021;**12**(1):1088 doi 10.1038/s41467-021-21246-9.

47. Na Z, Guo W, Song J, Feng D, Fang Y, Li D. Identification of novel candidate biomarkers and immune infiltration in polycystic ovary syndrome. *J Ovarian Res* 2022;**15**(1):80 doi 10.1186/s13048-022-01013-0.

48. Xie W, Cheng J, Hong Z, Cai W, Zhuo H, Hou J*, et al.* Multi-Transcriptomic Analysis Reveals the Heterogeneity and Tumor-Promoting Role of SPP1/CD44-Mediated Intratumoral Crosstalk in Gastric Cancer. *Cancers (Basel)* 2022;**15**(1) doi 10.3390/cancers15010164.

49. Avtanski D, Garcia A, Caraballo B, Thangeswaran P, Marin S, Bianco J*, et al.* Resistin induces breast cancer cells epithelial to mesenchymal transition (EMT) and stemness through both adenylyl cyclase-associated protein 1 (CAP1)-dependent and CAP1-independent mechanisms. *Cytokine* 2019;**120**:155-64 doi 10.1016/j.cyto.2019.04.016.

50. Qian W, Zhao M, Wang R, Li H. Fibrinogen-like protein 1 (FGL1): the next immune checkpoint target. *Journal of Hematology & Oncology* 2021;**14**(1) doi 10.1186/s13045-021-01161-8.

51. Jin X, Demere Z, Nair K, Ali A, Ferraro GB, Natoli T*, et al.* A metastasis map of human cancer cell lines. *Nature* 2020;**588**(7837):331-6 doi 10.1038/s41586-020-2969-2.

52. Dong M, Chen J, Deng Y, Zhang D, Dong L, Sun D. H2AFZ Is a Prognostic Biomarker Correlated to TP53 Mutation and Immune Infiltration in Hepatocellular Carcinoma. *Frontiers In Oncology* 2021;**11**:701736 doi 10.3389/fonc.2021.701736.

53. Bongiovanni L, Andriessen A, Silvestri S, Porcellato I, Brachelente C, de Bruin A. H2AFZ: A Novel Prognostic Marker in Canine Melanoma and a Predictive Marker for Resistance to CDK4/6 Inhibitor Treatment. *Front Vet Sci* 2021;**8**:705359 doi 10.3389/fvets.2021.705359.

54. Varghese AM, Perry MA, Chou JF, Nandakumar S, Muldoon D, Erakky A*, et al.* Clinicogenomic landscape of pancreatic adenocarcinoma identifies KRAS mutant dosage as prognostic of overall survival. *Nature Medicine* 2025;**31**(2):466-77 doi 10.1038/s41591-024-03362-3.

55. Tawbi HA, Schadendorf D, Lipson EJ, Ascierto PA, Matamala L, Castillo Gutiérrez E*, et al.* Relatlimab and Nivolumab versus Nivolumab in Untreated Advanced Melanoma. *N Engl J Med* 2022;**386**(1):24-34 doi 10.1056/NEJMoa2109970.

Downloaded from http://aacrjournals.org/clincancerres/article-pdf/doi/10.1158/1078-0432.CCR-25-3359/3748227/ccr-25-3359.pdf by guest on 01 April 2026

Figure legends

Figure 1. Single-cell transcriptomes of primary tumors and hepatic metastases in PDAC.

A, Schematic diagram of the study design to investigate metastasis-related factors using paired primary tumors (PTs) and hepatic metastases (HMs).

B, UMAP plot showing the celltype identities of scRNA-seq data from PTs and HMs.

C, Bubble plot showing the expression of marker genes for each major celltype in PDAC.

D, Box plots showing celltypes with higher frequencies in PTs. Paired one-sided Wilcoxon test.

E, Box plots showing celltypes with higher frequencies in HMs. Paired one-sided Wilcoxon test.

Figure 2. The C2 malignant subpopulation is highly plastic and associated with higher risk of hepatic metastasis.

A, UMAP plot showing 5 subclusters of ductal cells.

B, Bubble plot showing the top 6 highly expressed genes for each subcluster.

C, Functional annotations of the C0~C4 ductal subclusters.

D, Violin plot showing the CNV score for each subcluster. Unpaired two-sided Wilcoxon test, *P < 0.05; **P < 0.01; ***P < 0.001.

E, Pie plots showing the ductal subcluster compositions of PT and HM samples. Bar plots showing the ductal subcluster compositions of paired PTs and HMs within each patient. The cellular abundance of C2 is higher in HMs than in the corresponding PTs in 5 out of 6 patients.

F, Developmental trajectory of ductal subclusters inferred by Monocle2.

G, The C2 signature score is negatively associated with overall survival (OS) and disease-free survival (DFS) in the TCGA-PDAC cohort. +, censored observations; Log-rank test.

H, C2 signature scores of primary tumors from the TCGA-PDAC cohort with high or low hepatic metastasis risk. Unpaired single-sided Wilcoxon test. Signature scores were calculated using the Gene Set Variation Analysis (GSVA) method.

I, Hybrid EMT scores of all ductal subclusters calculated by AUCell.

J, Partial EMT scores of all ductal subclusters calculated by AUCell.

K, UMAP plots showing differentiation states and potency scores (red gradient) across all ductal cells.

L, Box plots comparing potency scores between cells from PTs and HMs, as well as between the C2 subcluster and other subclusters. Unpaired two-sided Wilcoxon test, *P < 0.05; **P < 0.01; ***P < 0.001.

Figure 3. Identification of *H2AFZ* as a major driver of malignant cell proliferation and metastasis.

A, Workflow for identifying key driver genes. Venn plot showing the intersection of signature genes of the C2 subpopulation, unipotent tumor cells with higher plasticity, and HM tumor cells.

B, Survival curves showing that the expression of *H2AFZ* was associated with worse OS and DFS in the TCGA-PDAC cohort. +, censored observations; Log-rank test.

C, Correlation between *H2AFZ* expression and C2 signature score in the TCGA-PDAC cohort. Each dot represents an individual sample. Spearman correlation.

D, H2AFZ exhibited higher expression in the HM tissues compared to paired PT tissues as validated by IHC. Paired two-sided Wilcoxon test.

Downloaded from http://aacrjournals.org/clincancerres/article-pdf/doi/10.1158/1078-0432.CCR-25-3359/3748227/ccr-25-3359.pdf by guest on 01 April 2026

E, H2AFZ exhibited higher expression in the highM group compared to the lowM group as validated by IHC. Unpaired two-sided Wilcoxon test.

F, Survival curves showing that the expression level of *H2AFZ* was associated with worse OS and DFS in our private data. +, censored observations; Log-rank test.

G, Correlation between *H2AFZ* expression and cell cycle score in the TCGA-PDAC cohort. Each dot represents an individual sample. Spearman correlation.

H, Expression level of H2AFZ was positively correlated with the level of MKI67 in human FFPE PDAC samples by IHC. Spearman correlation.

I, Cell viability of Patu8988 and SW1990 cell lines of the control and H2AFZ^{Si} groups by CCK-8 assay at the indicated time points. Unpaired, two-sided t test. $*P < 0.05$; $**P < 0.01$; $***P < 0.005$; $****P < 0.001$.

J, Representative images of colony formation assays and quantification of relative colony numbers in Patu8988 and SW1990 cells of the control and H2AFZ^{Si} groups. Unpaired, two-sided t test. $*P < 0.05$; $**P < 0.01$; $***P < 0.005$; $****P < 0.001$.

K, Representative images of transwell migration assays and quantification of relative migrated cells numbers in Patu8988 and SW1990 cells of the control and H2AFZ^{Si} groups. Unpaired, two-sided t test. $*P < 0.05$; $**P < 0.01$; $***P < 0.005$; $****P < 0.001$.

L, Representative images of liver metastases visualized by bioluminescence imaging system at weeks 2 and 4 after inoculating murine KPC^{Luc} cells.

M, Representative images of harvested livers with metastatic tumors. Visible lesions are outlined with red circles.

N, Bar plots showing the tumor burden measured by bioluminescence imaging at the experimental endpoint. Data are presented as mean ± SD. Unpaired, two-sided t test. $*P < 0.05$, $**P < 0.01$, $***P < 0.005$, $****P < 0.001$.

Figure 4. Hepatic metastases represent an immuno-suppressive microenvironment.

A, UMAP plot showing the myeloid subclusters.

B, Bubble plot showing the expression of marker genes for each myeloid subcluster.

C, Box plot showing the cellular abundance of C1QC+ macrophages and SPP1+ macrophages in hepatic metastases and healthy livers. HM, hepatic metastasis; HL healthy liver. Unpaired two-sided Wilcoxon test.

D, Bar plots showing the M1, M2 scores of all myeloid subclusters.

E, The developmental trajectory of monocytes and macrophages inferred by Monocle2 (Left). The M2/M1 scores for monocytes and macrophages along developmental trajectory (Right). The relative score was calculated as the M2 score divided by M1 score for each cell and subsequently scaled to a range of 0–1.

F, UMAP plot showing the T cell subclusters. Tc, cytotoxic T cell; Tn naïve T cell; Tex, exhausted T cell; Treg regulatory T cell. MAIT, mucosal associated invariant T cell.

G, Bubble plot showing the expression of marker genes for each T cell subcluster.

H, Box plot showing the cellular abundance of regulatory T cells and exhausted T cells in HMs and HLs. Unpaired two-sided Wilcoxon test.

I and J, Bubble plots showing ligand-receptor pairs that are strongest between the C2 ductal subcluster and immune subclusters increased in HMs compared with HLs, including C1QC+ macrophages, SPP1+ macrophages, regulatory T cells, and exhausted T cells. Interactions

Downloaded from http://aacrjournals.org/clincancerres/article-pdf/doi/10.1158/1078-0432.CCR-25-3359/3748227/ccr-25-3359.pdf by guest on 01 April 2026

between other ductal subclusters and these immune subclusters are comparatively weaker. The analysis was performed using CellChat.

Figure 5. Dual-blockade of PD1 and LAG3 represses the growth of hepatic metastases in murine metastatic models.

A, Heatmap showing the expression of cytotoxicity-related and immune inhibitory genes for each T cell subcluster within PTs and HMs.

B, Boxplot showing the expression levels of PD1 in paired PTs and HMs by IHC staining. Paired two-sided Wilcoxon test.

C, Boxplot showing the expression levels of LAG3 in paired PTs and HMs by IHC staining. Paired two-sided Wilcoxon test.

D, Line plot showing the tumor size measured by bioluminescence imaging at the indicated time points (days 3, 7, 14, and 21). Unpaired two-sided t test. $*p < 0.05$, $**p < 0.01$.

E, Bar plots showing the tumor size measured by bioluminescence imaging at the endpoint (day 21). The data are shown as mean ± SD. Unpaired, two-sided t test. $*p < 0.05$, $**p < 0.01$.

F, Representative images of liver metastases visualized by bioluminescence imaging system on day3, day7, day14, and day21 after inoculating murine KPC^{Luc} cells.

G, PCA plot showing the distribution of untreated control and treated mouse bulkRNA-seq data in the PC1 and PC2 dimensions.

H, Venn plot showing the intersection of genes upregulated after treatment.

I, Bubble plot showing the GO enrichment results of genes upregulated under different comparison conditions.

J, Heatmap showing the expression of immune and extracellular matrix related genes in untreated control and treated mice.

Figure 6. Schematic plot of the metastatic potential of PDAC tumor cells.

The PTs and HMs exhibit different cellular compositions in both tumor and immune compartments. Malignant subcluster C2 demonstrates the greatest metastatic potential to the liver among all malignant subclusters. T cells in HMs display a more exhausted state, characterized by higher PD1 and LAG3 expression in Tex cells compared with PTs.

Downloaded from http://aacrjournals.org/clincancerres/article-pdf/doi/10.1158/1078-0432.CCR-25-3359/3748227/ccr-25-3359.pdf by guest on 01 April 2026

Figure 1

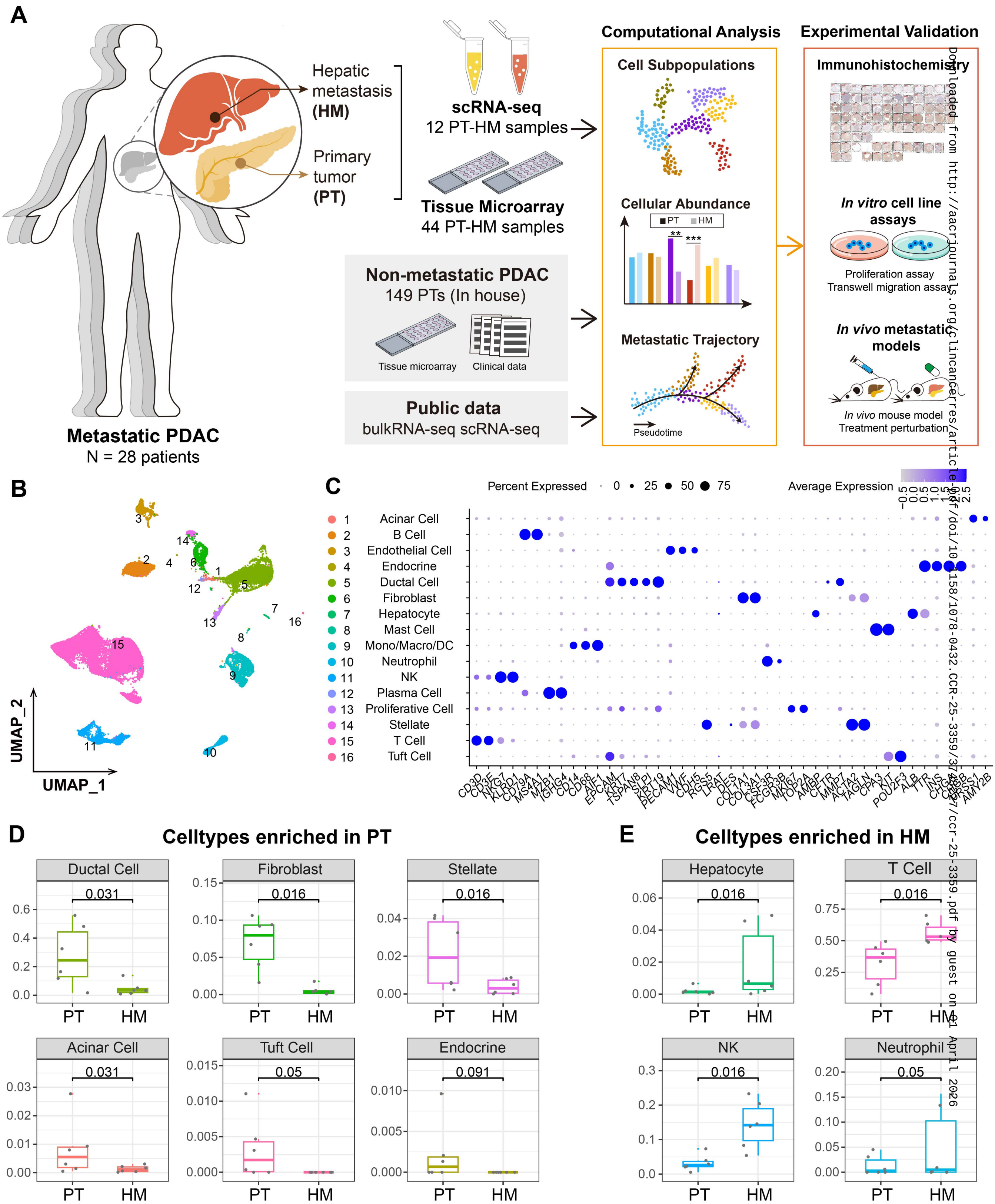

Downloaded from http://aacrjournals.org/clincancerres/article-pdf/doi/10.1158/1078-0432.CCR-25-3359/3746827/ccr-25-3359.pdf by guest on 01 April 2026

Figure 2

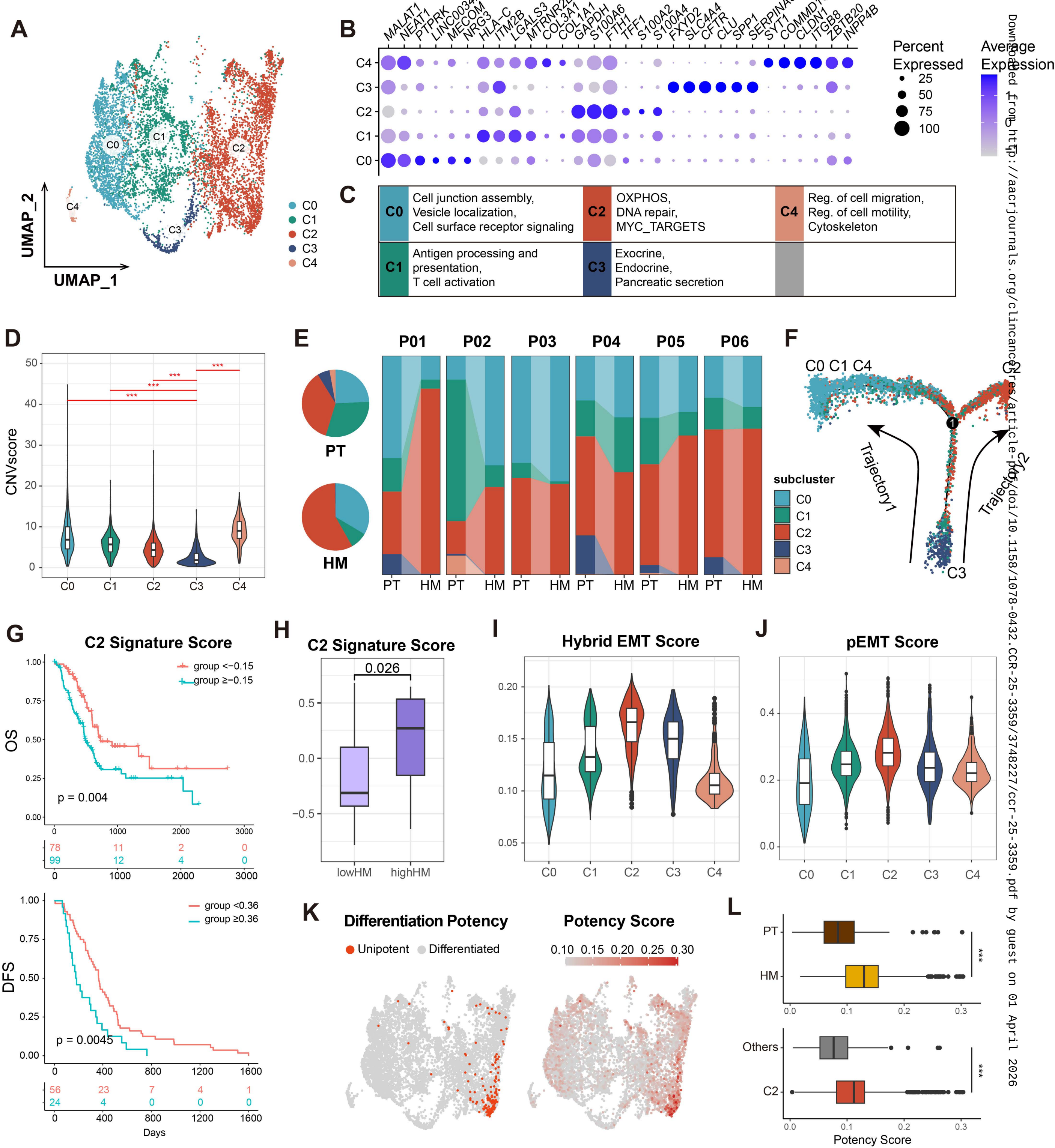

Downloaded from http://aacrjournals.org/clincancerres/article-pdf/doi/10.1158/1078-0432.CCR-25-3359/3748227/ccr-25-3359.pdf by guest on 01 April 2026

Figure 3

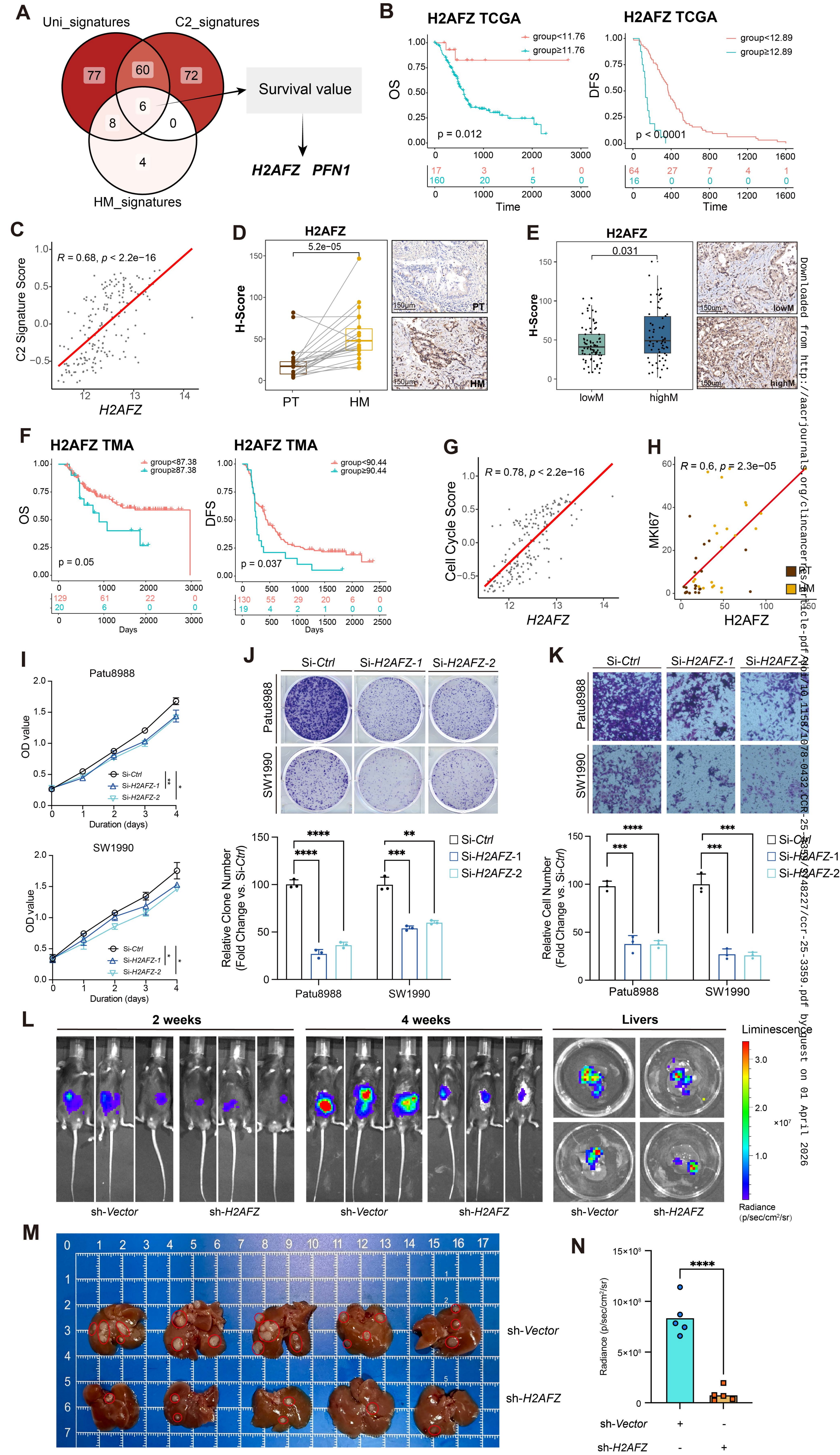

Downloaded from http://aacrjournals.org/clincancerres/article-pdf/doi/10.1158/1078-0432.CCR-25-3359/3748227/ccr-25-3359.pdf by guest on 01 April 2026

Figure 4

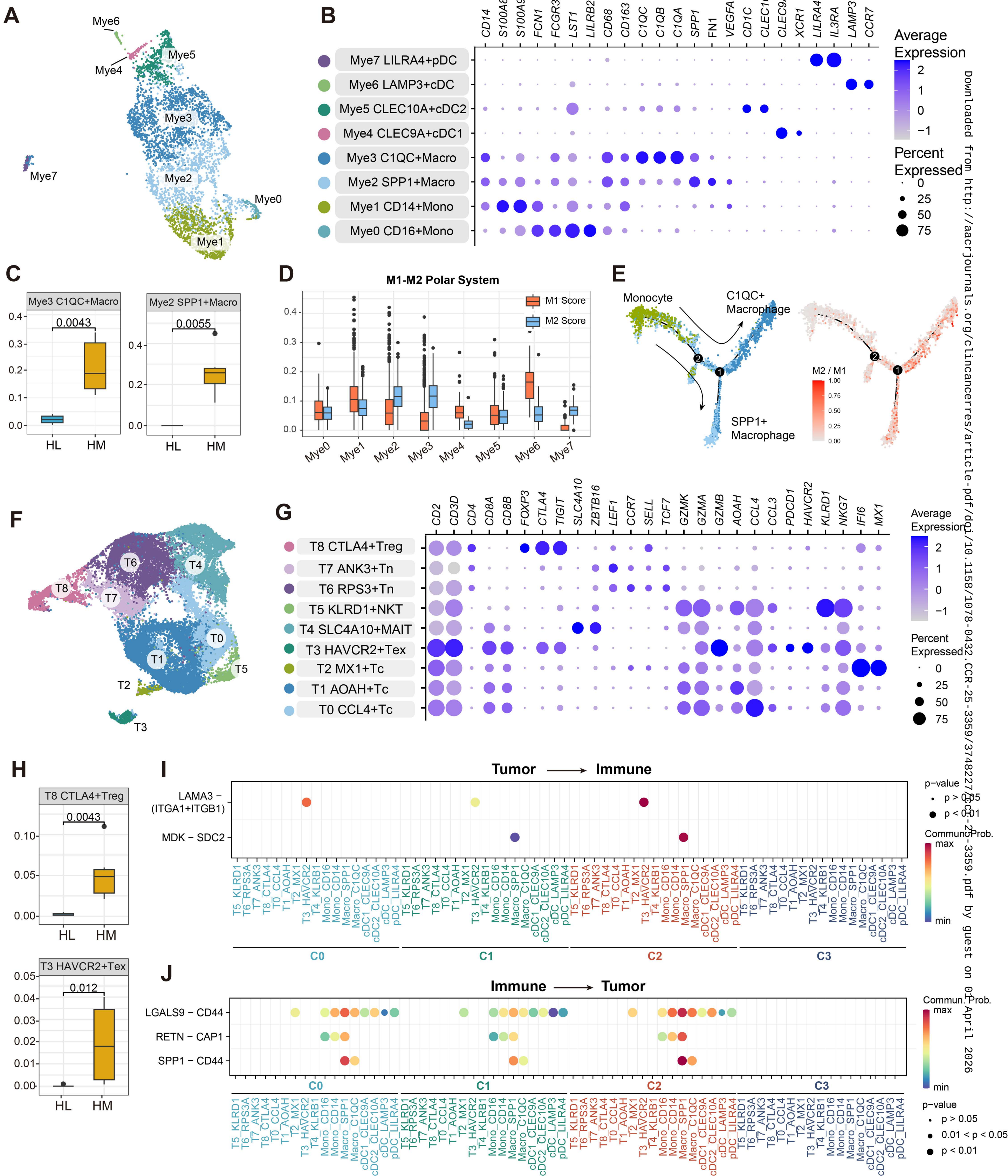

Downloaded from http://aacrjournals.org/clincancerres/article-pdf/doi/10.1158/1078-0432.CCR-25-3359/3748227/ccr-25-3359.pdf by guest on 01 April 2026

Figure 5

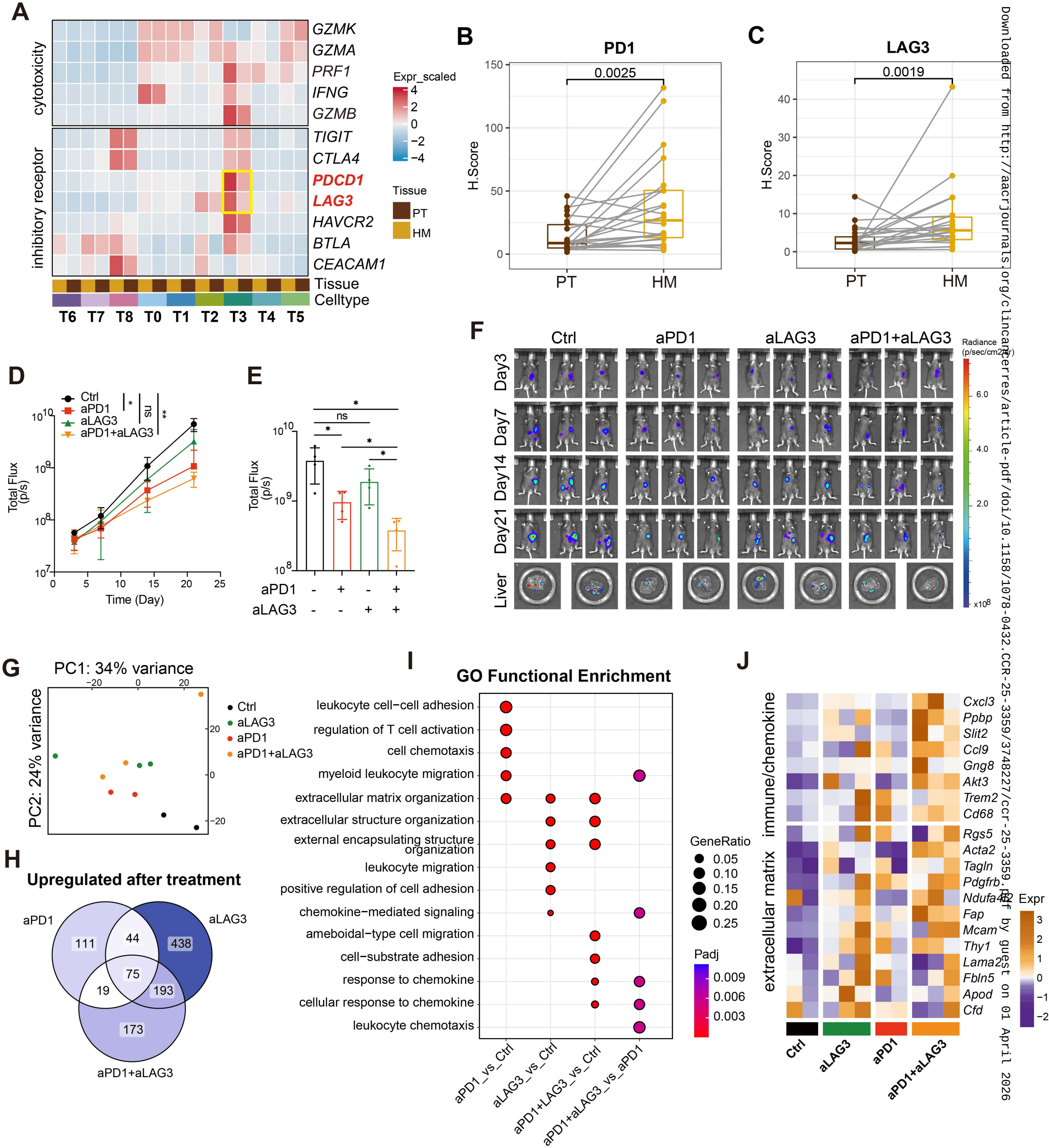

Downloaded from http://aacrjournals.org/clincancerres/article-pdf/doi/10.1158/1078-0432.CCR-25-3359/3748227/ccr-25-3359.pdf by guest on 01 April 2026

Figure 6

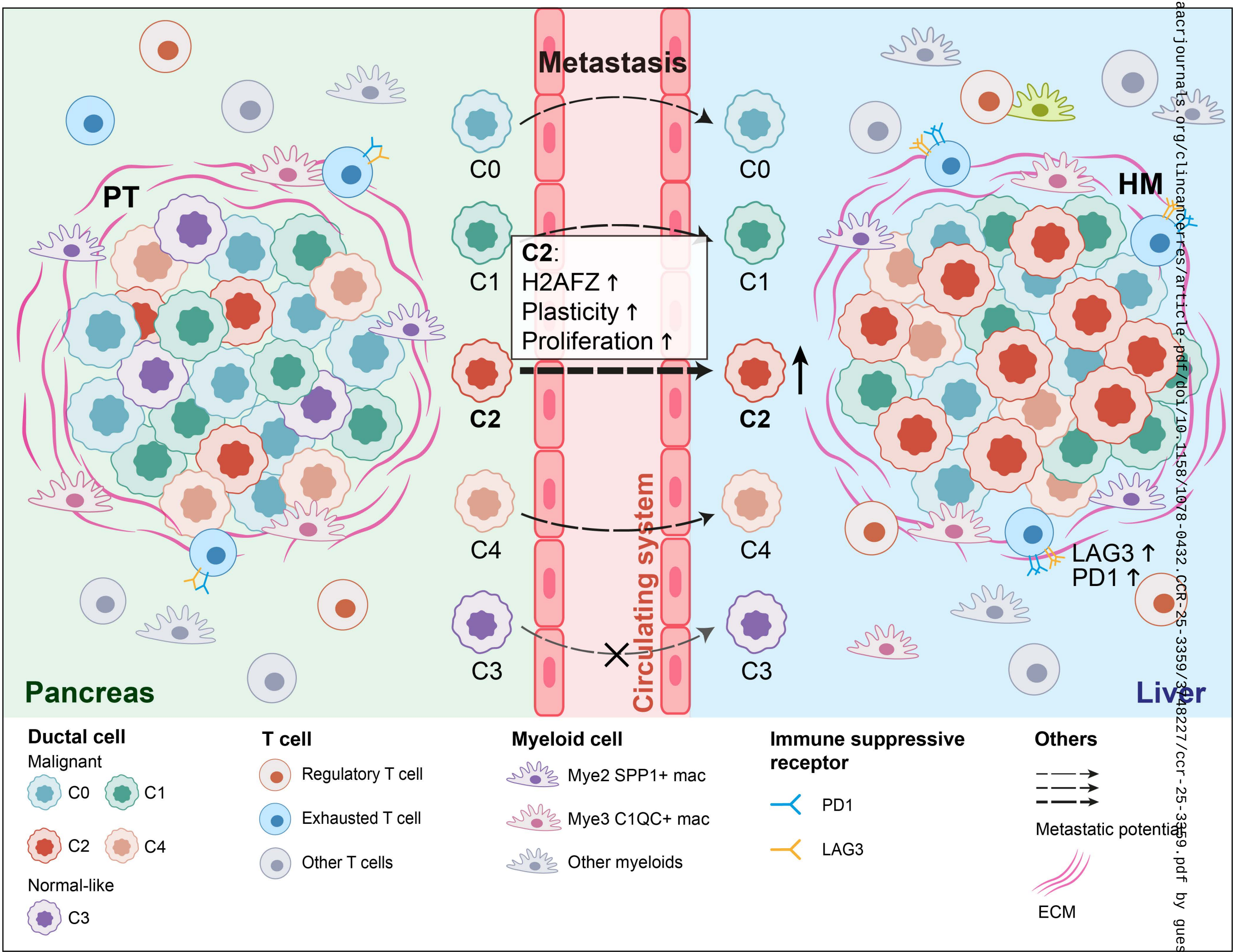

tp://aacrjournals.org/clincancerres/article-pdf/doi/10.1158/1078-0432.CCR-25-3359/3448227/ccr-25-3359.pdf by gues